Corrosion Science 174 (2020) 108809

Contents lists available at ScienceDirect

Corrosion Science

journal homepage: www.elsevier.com/locate/corsci

Elucidation of orientation relations between Fe-Cr alloys and corrosion products after high temperature SO_2 corrosion

Christiane Stephan-Scherb[a,b,*], Martina Menneken[a,c], Kathrin Weber[a,b], Leonardo Agudo Jácome[a], Gert Nolze[a]

[a] Bundesanstalt für Materialforschung und -prüfung (BAM), Unter den Eichen 87, 12205, Berlin, Germany
[b] Freie Universität Berlin, Department of Earth Science, Malteserstr. 74-100, 12249, Berlin, Germany
[c] Universität Bonn, Steinmann Institute of Geology, Meckenheimer Allee 169, 53115, Bonn, Germany

ARTICLE INFO

Keywords:
A. Iron
B. TEM
C. SEM
D. High Temperature Corrosion
E. Oxidation

ABSTRACT

The early stages of corrosion of Fe-Cr-model alloys (2 and 9 % Cr) were investigated after exposure at 650 °C in 0.5 % SO_2 containing gas by electron backscattered diffraction (EBSD) and transmission electron microscopy (TEM). The impact of the grain orientation of the base alloy on the orientation relations of the corrosion products is presented. After 2 min – 5 min exposure the formation of a multi-layered corrosion zone was discovered. A clear orientation relationship between ferrite and the $(Fe,Cr)_3O_4$ spinel could be demonstrated. The obtained results show the importance of the grain orientation on oxidation resistance.

1. Introduction

The surface degradation of metallic alloys is driven by a broad variety of factors that impact the corrosion and corrosion protection mechanisms. It is commonly known that alloying industrial alloys with chromium increases the oxidation resistance at medium to high temperatures (> 500 °C) due to the formation of a thin, fine-grained and dense chromia (Cr_2O_3) layer [1]. Ferritic-martensitic Fe-Cr alloys are widely utilized as materials for high temperature applications such as super heater tubes in coal, biomass or co-fired power plants [2,3]. These alloys contain up to 16 % Cr by weight and they generally support the formation of a Cr-rich oxide layer, providing further oxidation protection. Various corrosive gases are produced in combustion processes, but especially SO_2 is known to cause catastrophic failure of structural parts in technical applications [4,5].

When taking a step beyond these general considerations, the high complexity of the corrosion process becomes visible. Number of parameters influence the degradation and vast are the possible development paths until failure. The corrosion process must be understood both on a time scale and in terms of external and internal influences.

The process can be separated into multiple, time-dependent stages and each moment in time contributes to the outcome of the corrosion process. In the initial stage absorption and adsorption of the gas molecules are dominating the process and the steady-state oxidation is mainly driven by only one or two oxides. Especially in the early stages of oxidation, the grain boundaries and various grain sizes have a considerable influence on oxidation resistance, as demonstrated by Kim et al. for austenitic steels [6]. This study showed that oxides formed directly on grain boundaries in alloys with higher chromium content are enriched in chromium compared to oxides on grain faces.

To describe the growth kinetics of oxide layers, Cabrera-Mott and Wagner theory are frequently used [7,8]. Both theories assume planar and homogenous layer growth. Cabrera-Mott theory addresses an early stage of corrosion with oxide layers ranging from 1 to 10 nm thickness. Several studies were performed on single metal systems to study the initial reactions by high resolution techniques, even in the pre-Cabrera-Mott region [9,10]. As stated by other authors studying the hot corrosion of Ni-Cr alloys, nucleation and growth may occur rapidly in time periods of a few minutes to up to an hour [11]. Epitaxial relations between initial oxides and the underlying base alloys were recently demonstrated by Blades et al. for Ni-Cr alloys [10]. They demonstrated the oxidation of Ni–Cr leads to structural and compositional changes in the alloy surface itself and includes faceting of step edges by NiO growth, which is driven by the epitaxial relationship between the Ni–Cr and NiO lattices. Although the present study does not address the pre-Cabrera-Mott region, the analysis of epitaxial relationships between reaction products and the underlying base material is main objective. However, the structure, morphology and chemistry of oxide layers growing in the early stage of oxidation may add valuable insights to further optimize oxidation resistance of low alloyed ferritic steel.

* Corresponding author.
E-mail address: christiane.stephan-scherb@bam.de (C. Stephan-Scherb).

https://doi.org/10.1016/j.corsci.2020.108809
Received 11 February 2020; Received in revised form 8 June 2020; Accepted 9 June 2020
Available online 10 June 2020

A planar and homogenous growth as assumed by Cabrera-Mott and Wagner theory is not present for corrosion caused by the reaction of ferritic alloys with the aforementioned, potentially fatal SO_2 containing gas. Since SO_2 is known to strongly impact the overall oxidation process in various technical applications, it is of general interest to understand the intrinsic formation of protective oxide layers in environments that contain SO_2. For the case of SO_2 corrosion, the precursor oxides forming prior to the steady-state stage are not well characterized and the corrosion mechanisms in these states are not fully understood.

A previous study of the authors' group on the same Fe-Cr alloys studies the in-situ evaluation of oxidation-sulfidation mechanisms by real time in-situ EDXRD analysis showed signals of oxides immediately starting with gas exposure. The recording time was 30 s and it is assumed the initial oxidation happens in an exposure time of < 1 min [12]. No potentially protective chromia was revealed in that study, only Fe- and Fe,Cr-mixed oxides. A better understanding of the corrosion process start in this material class can lead to the development of strategies facilitating the formation of more protective Cr-enriched oxide layers.

External (gas, pressure, temperature) and internal (material composition, chemical potential, grain size, level of deformation, particle orientation) influences are manifold and each of them influences each other's. The study of only one of them requires a strict control of the other parameters. In the case of chromia, for example, its formation and its stability do not only depend on the chemical potential of chromium in the alloy. Even in pure chromium the formation and stability of chromia layers are affected by temperature and the oxygen partial pressure, which influences the defect properties of Cr_2O_3 [1,13–15]. Additionally, microstructural factors allowing short diffusion paths for the chromium towards the alloy/gas interface affects the formation of chromia as a protective layer. This was demonstrated by Kim et al., who studied the role of grain boundaries in the initial oxidation behaviour of austenitic-stainless steel at 700 °C, and showed that grain size refinement is an advantageous approach to increase oxidation resistance to high temperature oxidation [6].

There have been extensive studies examining the impact of SO_2 content for both Fe-Cr alloys and Cr-Mn steels in single and mixed gas environments at long exposure times [16–19].

An early study by Kirsch showed that the corrosion layers on steel pipes after reaction with water vapor and steam represent a pseudomorphosis from magnetite to steel [20], indicating that the initial corrosion mechanisms mainly depend on the presence of oxygen, and are not changed in the presence of sulphur. However, sulphur is incorporated into the oxide scale in the low chromium containing alloy, and mainly observable in the inner corrosion zone for the higher alloyed material [18]. During oxidation of iron at 220 − 450 °C, Boggs et al. [21] observed in an oxygen partial pressure between 0.1317 Pa and 1.317 Pa the formation of cubic magnetite as first phase. Sewell and Cohen [22] investigated the oxidation of iron single crystals at 200 °C and found an increased oxide volume for the low indexed base planes {100}, {110} and {111} as opposed to higher indexed planes. During heat treatment at 627 °C Fe-Cr alloys with 5–20 % Cr and an oxygen partial pressure of 131.7 Pa–101325 Pa, Leygraf and Hultquist [23] studied the early stages of oxidation on Fe-Cr (100) and (110) single crystals between 700 and 900 K. The first phase revealed the rhombohedral $(Fe,Cr)_2O_3$, which showed epitaxial growth of $\{0001\}_{(Fe,Cr)2O3} \,||\, \{110\}_{\alpha\text{-}Fe}$. The authors stated that the most probable adsorption sites of oxygen are the centres of the (100) – ferrite plane. As soon as all centres are occupied by oxygen, a monolayer of a film with *fcc* symmetry forms with $(100)_{magnetite} \,||\, (100)_{ferrite}$. The *fcc* type oxide acts as a base for further spinel oxide formation during prolonged oxidation. Next to the epitaxial relations evaluated here, other aspects influencing the oxide layer growth in an early stage must be taken into account. [24] showed on an Inconel 617 exposed for 300 s at 700 °C to 101325 Pa CO_2 the coalescence of cation vacancies in the alloy at the alloy/oxide interface leading to a low-density region below the oxides [24,25]. This kind of vacancy coalescence can be assumed to be present during the early oxidation of metals in SO_2 containing atmosphere, too. Nevertheless, the arrangement of iron and oxygen atoms has an underestimated effect, particularly in the early stages of corrosion.

Despite these numerous studies on different aspects of the Fe-Cr corrosion, there is a lack in knowledge of the microstructural aspects of the underlying base material. One of the rare studies is the one by Juricic et al., who studied at 650 °C the evolution of microstructure and internal stresses in oxide layers grown on (110) surfaces of iron single crystals [26]. Tensile and compressive stresses were measured at the various interfaces between magnetite, wüstite and hematite. The stresses caused by the volumetric differences between the different iron oxides are the sources for the stress formation. The present work aims at increasing the knowledge on microstructural considerations and highlights the importance of the grain orientation of the Fe-Cr alloy on the chemical and structural properties of the corrosion products in the early stages of SO_2 corrosion.

To understand the effect of grain orientation and chromium content on the phase formation, coupons of Fe-Cr model alloys were analyzed using electron backscattered diffraction (EBSD) before and after exposure to SO_2. Additionally, EBSD analysis after corrosion experiments provides much needed insight in the crystalline nature of the corrosion products. This correlative approach enables the visualization of the preferential and grain orientation dependent growth of corrosion products and can easily be transferred to other similar scientific questions such as the understanding of aqueous induced corrosion mechanisms. Very thin corrosion layers as observed after short exposure times, are a prerequisite for collecting high quality EBSD data. The aim of this work is thus to elucidate the orientation relationships between ferrite and the oxidation products observed after short SO_2 exposure and to demonstrate the possibilities of applying surface EBSD after corrosion. By understanding the impact of the surface's crystal orientation(s) on the development of a Cr-rich layer, a path is set for the possibility of engineering crystallographically textured grains at the surface which enable and/or enhance the formation of layer that is more protective than the predominant magnetite and hematite.

2. Material and methods

2.1. Material pre-treatment and oxidation tests

Iron based model alloys were commercially purchased from *HMW-HAUNER Metallische Werkstoffe*. After cold working, the material was heat treated by the manufacturer at 800 °C for 8 h to recover and to coarsen the grains. 99.99 percent by weight purity is guaranteed by the manufacturer for each alloying element. Optical emission spectrometry (OES) was applied to specify the composition (see Table 1). The obtained metal sheets were cut into 15 × 20 mm rectangular coupons with 3 mm in thickness. Prior to the oxidation tests, each specimen side of the coupons was ground with SiC paper up to 1200 grit then polished to 1 µm particle sizes and finally cleaned in ethanol. For each sample, Vickers indents acted as markers to guarantee inspection of the same area before and after the oxidation experiment. Prior to EBSD analyses the sample surface was additionally polished with MasterMet™ 2 colloidal silica suspension. The surface was characterized by EBSD maps, after which the samples were immediately transferred to an infra-red

Table 1
Overview of the material composition measured by optical emission spectrometry (OES) and times of the SO_2 exposure.

Material	Fe-content [%] in weight	Cr-content [%] in weight	Mn-content [%] in weight	Exposure time [min]
Fe2Cr0.5 Mn	97.4 (1)	2.0 (1)	0.5 (1)	2
Fe9Cr0.5 Mn	90.1 (1)	9.2 (1)	0.5 (1)	5

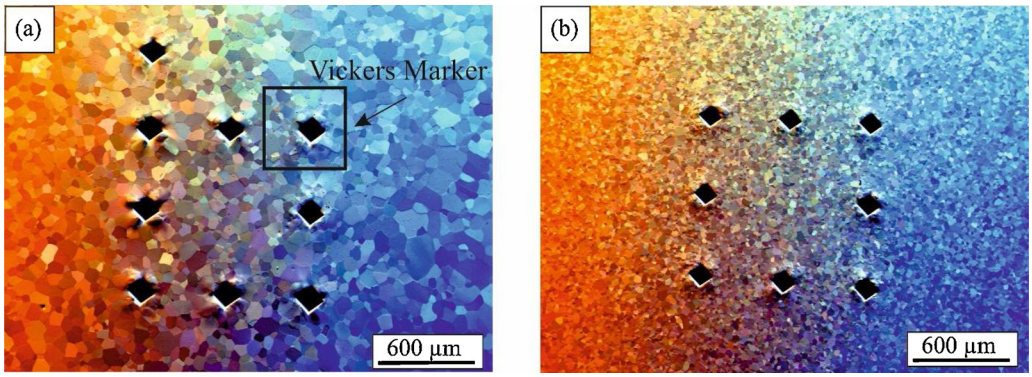

Fig. 1. SEM images (for scattered electron detector, 70° tilted sample surface) comparing the microstructures of the studied model alloys a) Fe2Cr0.5 Mn and b) Fe9Cr0.5 Mn. The black squares indicate the Vickers indents used as markers. The high sample tilt in combination with the tilt compensation generates an exaggerated topography around the Vickers indents.

(IR) light furnace where isothermal (T = 650 °C) experiments were performed to different times (Table 1). The furnace is dedicated to short time exposure experiments, as will be described in the following chapter.

The reactor setup consists of a gas flow system inside a steel container with four infrared radiators. A gas mixture of 0.5 % SO_2 and 99.5 % Ar was used with a constant flow rate of 1.1 L min^{-1} with a gas velocity of 0.001 m·s^{-1} at the samples. The gas flow was parallel to the sample and a thermocouple was placed inside each metal sheet to control the sample temperature and to regulate the power of the IR-radiators to a constant sample temperature of 650 °C. Heating and cooling took place under pure Ar flow. A detailed description of the furnace is given elsewhere [18]. The integrated water-cooling system of the furnace especially enables fast cooling of the samples and thus allows to immediately stop the development of oxidation products, freezing the current state. An exposure time of only 2 min was chosen for Fe2Cr0.5 Mn to avoid complete coverage of the surface by reaction products and to focus on the early stage of degradation. For Fe9Cr0.5 Mn a reaction time of 5 min was necessary to visualize by scanning electron microscopy the early stages of oxidation and corrosion. Longer exposure experiments were additionally conducted. However, these experiments are not implemented in the present study, since with increasing exposure time, the topography of the oxide layers increases strongly, and shadowing effects influence the significance of the surface EBSD analysis.

2.2. Characterization methods

The EBSD analyses (ESPRIT 1.94, Bruker Nano) were performed in a scanning electron microscope (SEM) *Leo 1530 VP (Zeiss)* at an acceleration voltage of 20 kV using an $e^{-}Flash^{HR}$ detector. Prior to EBSD analyses, the energy-dispersive x-ray spectroscopy (EDS) signal was collected for a chemical analysis using an XFlash 5030 (ESPRIT 1.94, Bruker Nano).

After the ageing experiment, a lamella of the corrosion layer was prepared for transmission electron microscopy (TEM) using a focused ion beam microscope (FEI FIB Quanta 3D FEG). Thinning of the lamella started with 30 kV and was decreased to 2 kV as final polishing step. The TEM investigations were performed in a JEM-2200FS microscope (JEOL, Japan) with a field emission gun and operated at 200 kV. The TEM was equipped with an in-column energy filter, a scanning unit with a bright field high-angle annular dark field detector, and an EDS system (JEOL, energy resolution: 138 eV).

2.3. Data post-processing for grain analysis

To prove the suggested orientation relations between oxidation products and the underlying ferrite, as observed by EBSD, a detailed analysis procedure was applied to randomly chosen grains. The analytical sequence for the EBSD maps collected before and after gas exposure was as follows:

1) Individual grains were isolated from the map by local area selection.
2) All orientations except of the major ones were removed to delete all solutions from adjacent grains, misorientations and other aspects impacting the orientation.
3) Again, all solutions are included within the grain by selecting an area smaller than the visual grain shape.
4) Removement of orientation scattering in pole figures. They are very likely caused by pattern misinterpretations, multiple twinning or random nucleation so that these orientations do not fit to the interface.
5) Individual separation of the remaining 2 or 3 major orientations.
6) Convolution of pole distributions.
7) Pole figures of oxides were overlaid by ferrite using transparency.
8) Indication of most likely parallel (hkl) and [uvw] by black or colored circles according to the assumed relationships between {001}, {110} and {111}.

3. Results

3.1. Alloy microstructure before corrosion

In order to evaluate the surface oxidation, all samples were analyzed before and after the ageing experiment by EBSD. Fig. 1 depicts the sample surfaces and their microstructure before the exposure tests. Vickers indenting (see Fig. 1 black rhombic areas) was used to mark defined positions on the surface for inspection. By this it was possible to collect EBSD orientation maps at exactly the same position before and after exposure to the reactive gas.

3.2. Alloy surfaces after corrosion

Since Fe2Cr0.5 Mn and Fe9Cr0.5 Mn show a closed oxide layer after 2 min and 5 min respectively, the EBSD study focuses on these samples. SEM images (Fig. 2) demonstrate that after short time exposure at 650 °C with 0.5 % SO_2 a considerable change of the sample surface arises. Already 2 min are sufficient to cover the surface of Fe2Cr0.5 Mn completely by an oxide layer (see Fig. 2 (a)). Grain boundaries are often decorated, but the differently oriented substrate grains become also distinguishable by the various morphology of the crystals forming the oxide layer. Solid white lines are used to mark substrate grains which show bigger oxide grains on top. For Fe9Cr0.5 Mn, after 5 min of oxidation the alloy is covered completely by a thin oxide layer. The oxidised surface appears smoother, compared to Fe2Cr0.5 Mn, with locally occurring topological outbreaks. The solid line marks grains with a honeycomb like surface structure, whereas the dotted line demonstrates grains with a very fine grained and thin oxide. The different morphologies suggest a clear impact of the grain orientation of the base alloy on the oxide scale formation.

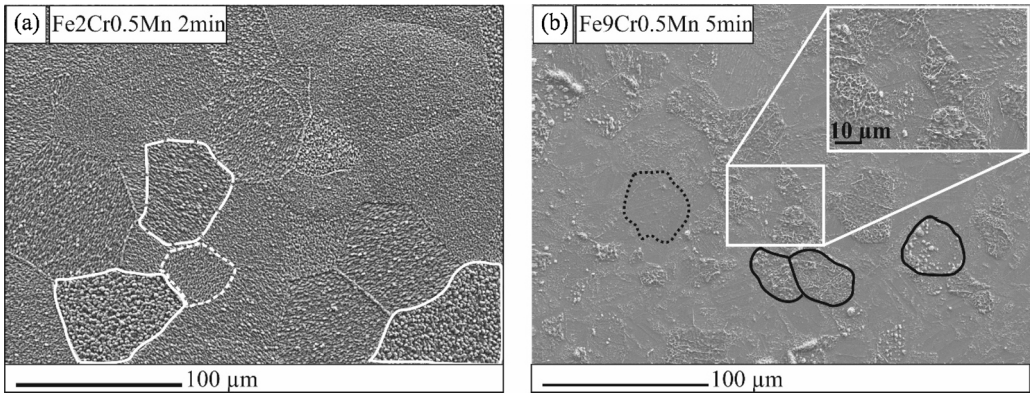

Fig. 2. Secondary SEM images of alloy surfaces after oxidation of (a) Fe2Cr0.5 Mn and (b) Fe9Cr0.5 Mn. Selected grains are marked by solid, dashed and dotted lines to illustrate different surface morphologies of the oxide layer for different grains.

3.3. Surface characterization by EBSD

3.3.1. Fe2Cr0.5 Mn

The surface description is defined by a reference direction which is commonly parallel to the sample normal (z-direction). Fig. 3 (a) shows the EBSD orientation map of Fe2Cr0.5 Mn in z-direction (at the surface) of the ferrite before exposure. The corresponding EBSD orientation map in z-direction of the oxide after the reaction with SO_2 is shown in Fig. 3 (b). The crystallographic description is encoded by a colour key. However, 'red' does not mean [001], it covers a bigger angle range which is toward [101] ± 10°and towards [111] ± 15°. This means, reddish colored grains may have misorientations between 20° to 30°. Clearly, each ferrite grain shows oxide grains with similar orientation. An EBSD phase map of the grown oxide layer at the same position after exposure reveals from a suggested list of corrosion products (Cr_2O_3, Fe_2O_3, FeS, Fe_3O_4) magnetite (Fe_3O_4) as the top oxide. Magnetite forms a closed layer on top of ferrite, independent of the orientation.

The comparison of the two maps collected before (pre-ox) and after (post-ox) gas exposure directly demonstrate the following aspects.

A) The top oxide is magnetite with an orientation relation to ferrite.
B) The post-ox map contains some non-indexed values (black points), which may be explained by the orientation scattering of magnetite to ferrite.

Only a few crystals are in the measured area. Nevertheless, to prove the suggested relationship a detailed grain analysis was performed on 8 grains. Despite only a small number of grains being analyzed, the observations indicate the concept described below. The analytical sequence for this procedure is summarized in the experimental part. The following results are presented for one exemplary case.

The maps displayed in Fig. 4 demonstrate the orientation map of magnetite. The figure represents three different views of the same orientation measurement of magnetite, displaying the crystallographic indexing of the horizontal (x), the vertical (y) and the normal direction of the hosting sample stage (z). Fig. 3 (a + b) display a map detail of Fig. 4 (IPF-Z). According to Fig. 3 (a) the surface orientation of ferrite before the gas exposure of the grain A is about 5° away from [110]. Comparing the orientation of magnetite on the surface after gas exposure displayed in Fig. 4, the main obvious observation is:

Magnetite with [111] in z-direction grows on ferrite with [110]. The description is $\{110\}_{Fe} \| \{111\}_{Mag}$

This grain is marked with A in Fig. 4 and Fig. 3. For this orientation relations, twins can be observed, too (IPF-Y map, blue – magnetite {111} and its twin in pink). The oxide structure formed on the alloy follows the law of closed packing of lattice planes. The parallelism of the closed packed planes is not perfect as seen by remarkable misorientations of the magnetite crystals. Comparing the pole figures of ferrite and magnetite, two of the $\{110\}_{Fe}$ have a comparable deviation to the surface plane. The corresponding $\{111\}_{Mag}$ (see Fig. 4 - magnetite pole figures) grow with the same misorientation. The pink pixels in the magnetite {111}- pole figure are real orientations, defining the twins for both $\{111\}_{Mag}$. Depending on the selection of the active $\{110\}_{Fe}$, a different fit of the growing magnetite crystals result.

According to the symmetry of the ferrite, further magnetite orientations occur, but the obviously determining orientation relationship during oxidation is $\{110\}_{Fe} \| \{111\}_{Mag}$.

3.3.2. Fe9Cr0.5 Mn

Starting with the EBSD analysis before the gas exposure, where it was unknown at which position acceptable results will be generated after oxidation, at first a bigger area at lower resolution was measured. Fig. 5 (a) and (b) represents again the crystallographic indexing of the sample normal direction (IPF-Z) for Fe9Cr0.5 Mn alloy before and after exposure to the SO_2 containing gas. An EBSD phase map of the grown oxide layer at the same position after exposure reveals from a suggested

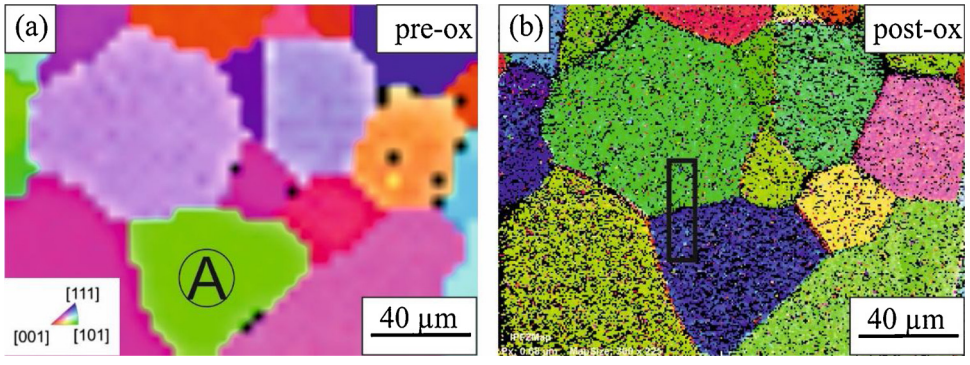

Fig. 3. Crystallographic indexing of the sample normal direction of Fe2Cr0.5 Mn before (a) and after corrosion (b) using EBSD. The EBSD maps display the normal direction of the hosting sample (IPF-Z). The black rectangle marks the position of the TEM lamella prepared by FIB. On the ferrite grain A in green [101] magnetite in blue [111] is observed.

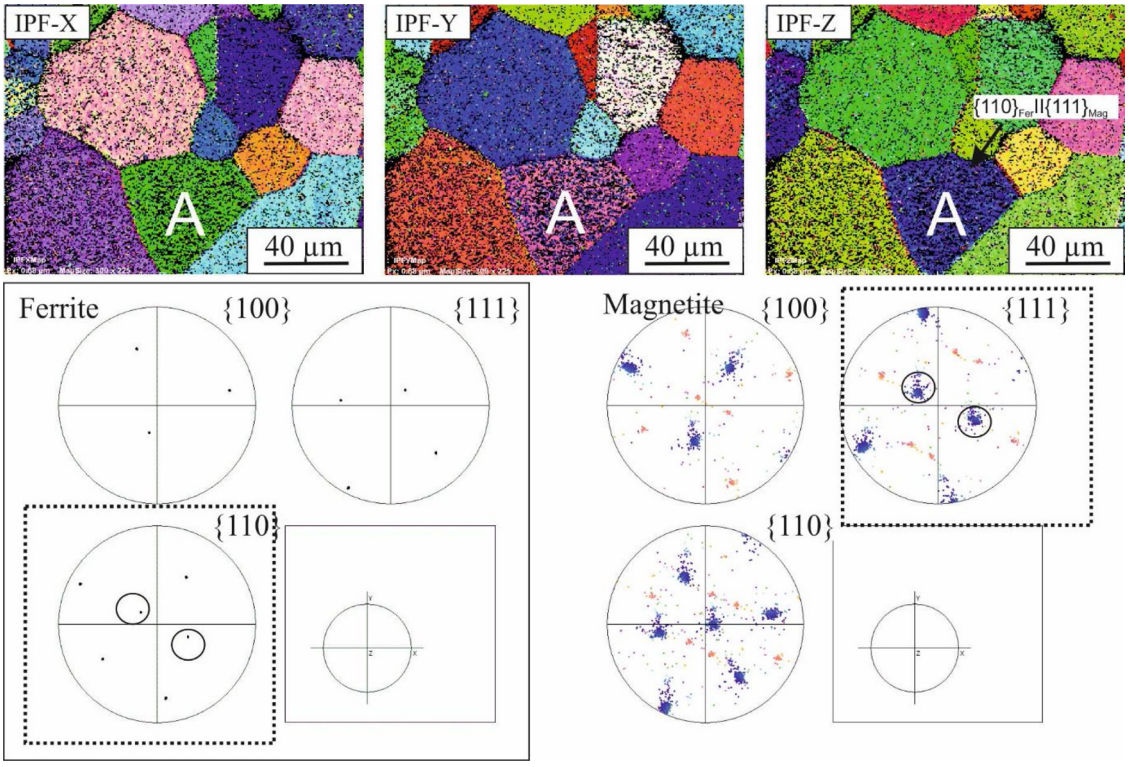

Fig. 4. EBSD orientation maps in x-, y-, and z-direction of magnetite grown on Fe2Cr0.5 Mn after 2 min of exposure to 0.5 % SO_2 atmosphere at 650 °C. In the lower part of the figure corresponding pole figures are displayed. In the IPF-Z map, grains with the orientation relation of $\{110\}_{Fe}\|\{111\}_{Mag}$ is marked by the black arrow and the correspondence in the pole figures by a black circle.

list of corrosion products (Cr_2O_3, Fe_2O_3, FeS, Fe_3O_4) hematite (Fe_2O_3) as the top oxide (see Fig. 5 (d)). The EBSD orientation distribution maps show correlations before and after the gas exposure. Some grains remain in shape and size, whereas other split into multiple grains with different orientations. However, some orientation relations can be determined. The observations can be summarized as follows:

- The oxide layer on top of Fe9Cr0.5 Mn after exposure to SO_2 is hematite.
- Hematite grows on magnetite, and magnetite on ferrite. The orientation relation between hematite and magnetite has priority. Nevertheless, the surface of ferrite grains with [101]-orientation prior oxidation (green grains in Fig. 5 (a) and (b))) develop a

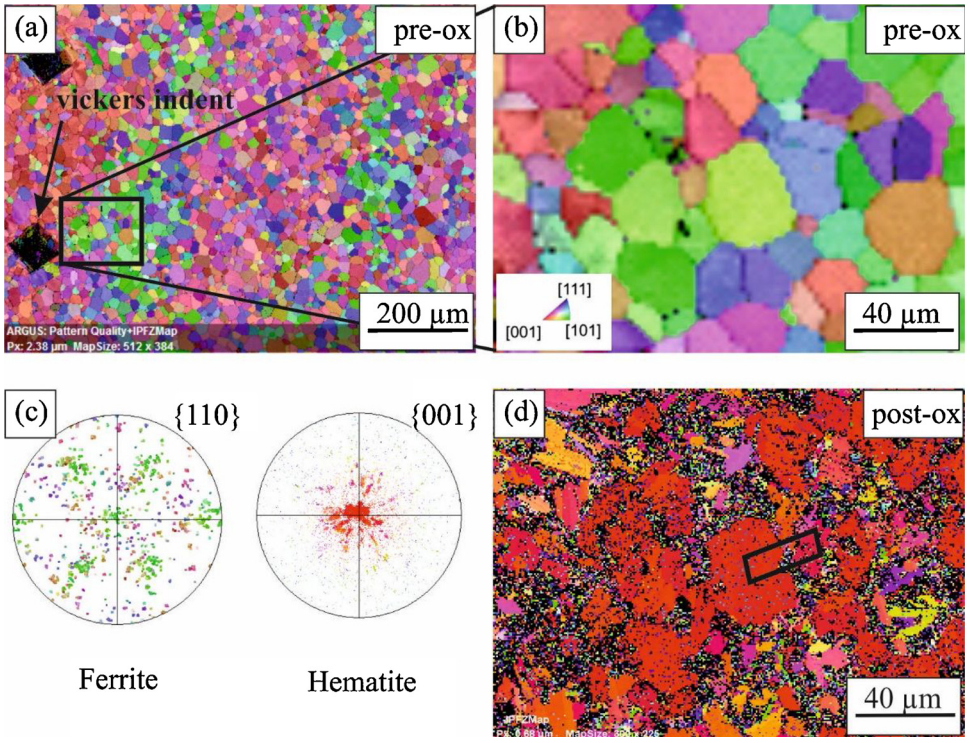

Fig. 5. Map of the crystallographic indexing of the sample normal direction for Fe9Cr0.5 Mn before (a); (b) and (d) after exposure to 0.5 % SO_2. (c) Represents the pole figures for ferrite and hematite corresponding to the defined orientation relation. The black rectangle in (d) marks the location of the TEM lamella as lift-out by the FIB technique.

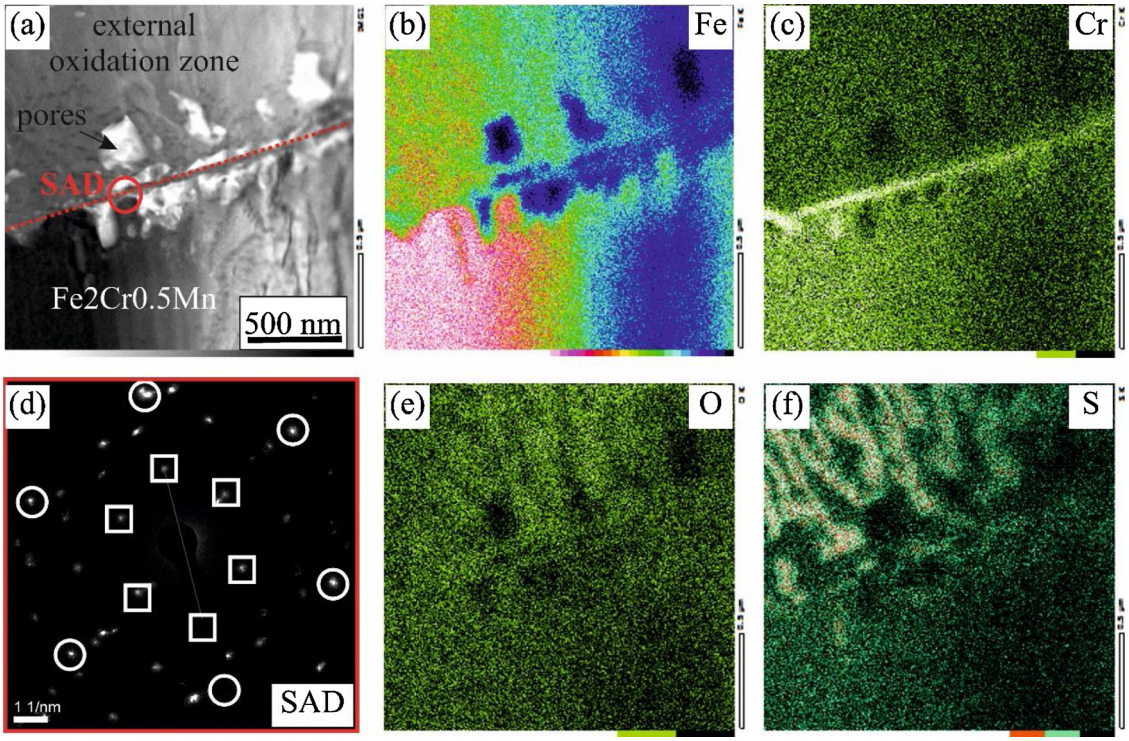

Fig. 6. STEM cross-sectional analysis of the corroded surface of Fe2Cr0.5 Mn after 2 min of exposure to 0.5 % SO_2 at 650 °C. (a) STEM bright field image and (b), (c), (e) and (f) EDS elemental distribution maps of the area shown in (a). The red dotted line marks the original sample surface. The red circle in (a) shows the area the SAD pattern shown in (d) was collected. Within this SAD pattern the circles correspond to ferrite and the squares to spinel reflections. (For interpretation of the references to colour in this figure legend, the reader is referred to the web version of this article).

hematite layer with clear [001]-orientation.

- The hematite grains are significantly smaller, compared to the substrate (ferrite) grains, if the ferrite orientation is not close to [101]. This behaviour was not observed for magnetite grown on Fe2Cr0.5 Mn.

3.4. TEM-analysis

3.4.1. Fe2Cr0.5 Mn

The EBSD analysis resulted in a comprehensive understanding of the oxide layer at the oxide/gas interface. In order to analyze the microstructure and composition of the grown layer in depth, a further TEM analysis was performed on a cross section. A lamella was cut out by the FIB lift-out technique across a grain boundary between two ferritic grains with magnetite and $\{111\}_{Fe}\|\{110\}_{Mag}$ and $\{110\}_{Fe}\|\{111\}_{Mag}$ indexing (see Fig. 3 (b)). Fig. 6 shows the TEM-EDS mapping of Fe, Cr, O and S of layers grown on $\{110\}_{Fe}$. The outer layer has a thickness of < 1 µm close to the gas interface consists of Fe_3O_4, as determined by EBSD, and S-enriched regions. Since crystalline sulphides were not observed by EBSD and in the selected area diffraction (SAD) pattern of this area (not shown here), the S-enrichment displays the initial nucleation of iron-sulphides within a Fe_3O_4 matrix (Fig. 6 (f)) rather than crystallised sulphides as observed after longer exposure times [15,18]. Along the former sample surface (red dashed line in Fig. 6(a)), a thin Cr-enriched layer can be observed. It cannot be verified, whether this is already an initial chromia (Cr_2O_3) layer. The SAD pattern (see Fig. 6 d)) of the Cr-rich layer indicates more a spinel type crystal structure corresponding to chromite or Cr-enriched magnetite. The Cr-rich zone seems to not be protective, as several pores are found below this layer, indicating material loss in this area. In the inner oxidation zone sulphur and chromium enrichment indicates the initial state of precipitation of Cr-sulphides as they are clearly observed after longer exposure times [18]. The layer stacking of reaction products as presented for $\{110\}_{Fe}$ from the alloy to the gas side is: Fe2Cr0.5 Mn/(Fe,Cr)-spinel/Magnetite with sulphur enrichment. This stacking is occurring independently from the initial ferrite orientation. The grain orientation of ferrite doesn't affect the resulting stacking of corrosion products.

3.4.2. Fe9Cr0.5 Mn

As for Fe2Cr0.5 Mn the lift out of a lamella took place at a region covering $\{110\}_{Fe}$ and $\{111\}_{Fe}$ ferrite grains. This lamella was further studied by TEM. Fig. 7 summarizes the cross-sectional STEM analysis of the corrosion layers. The bright field image in Fig. 7 (a) shows a two-phase outer corrosion zone with a thickness of about 500 nm and a porous inner corrosion zone. According to the SAD pattern and the elemental distribution, the outer zone consists of hematite and magnetite. The EDS elemental distribution illustrates again a chromium-rich layer at the original samples surface. This layer was identified by SAD as a spinel type Fe-Cr-oxide with a high degree of porosity. The presented area displays a small sample volume, but the pores are clearly visible over a larger sample area. This illustrates the very early stage of pore formation induced by combined oxidation/sulfidation. Sulphides, expected to be agglomerated at the scale/alloy interface, were not observed in this material (7).

4. Discussion

The chemical and structural layer stacking as observed by EBSD and TEM is illustrated in Fig. 8. The presented SEM-EBSD and TEM characterization after the short exposure of two ferritic alloys in hot SO_2 containing atmosphere demonstrated the following layer stacking of oxides.

- Fe2Cr0.5 Mn: Alloy/Cr-rich $(Fe,Cr)_3O_4/Fe_3O_4$.
- Fe9Cr0.5 Mn: Alloy/Cr-rich $(Fe,Cr)_3O_4/Fe_3O_4/Fe_2O_3$

Sulphur accumulation was found on Fe2Cr0.5 Mn in the external corrosion zone. For both alloys, from thermodynamic considerations,

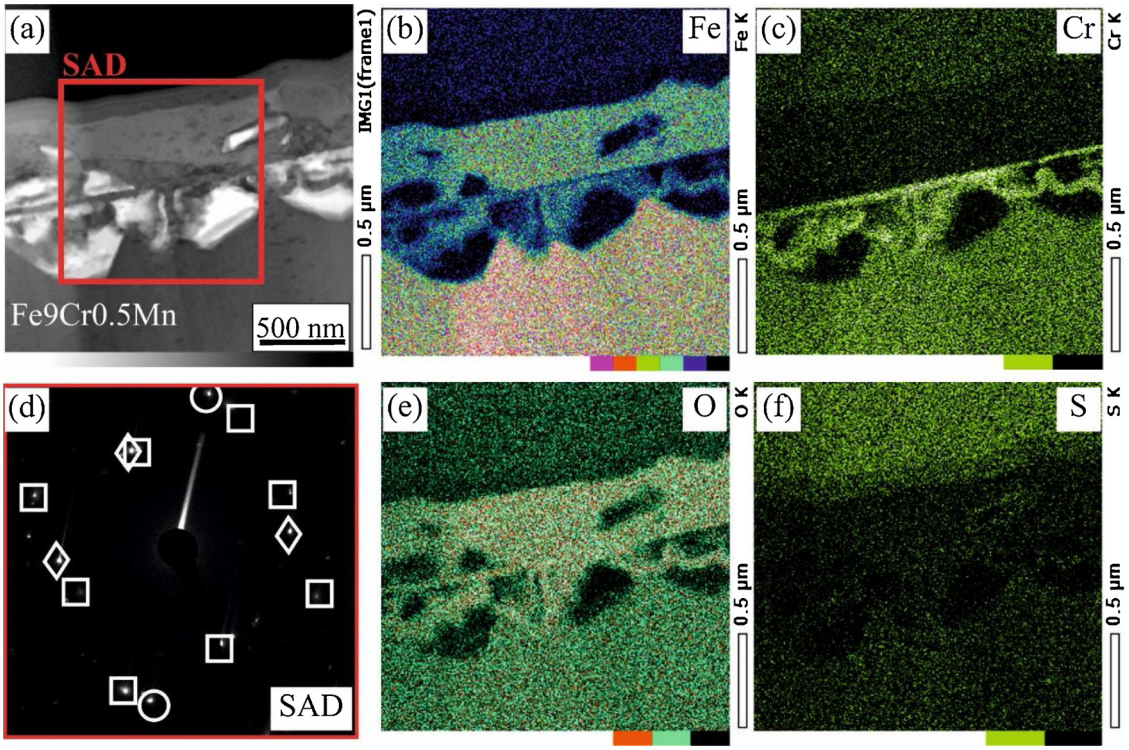

Fig. 7. STEM cross-sectional analysis of the corroded surface of Fe9Cr0.5 Mn after 5 min of exposure to 0.5 % SO_2 at 650 °C. STEM bright field image and (b), (c), (e) and (f) EDS elemental distribution maps of the area shown in (a). The red dotted line marks the original sample surface. The red circle in (a) shows the area the SAD pattern shown in (d) was collected. Within this SAD pattern the circles correspond to ferrite, the squares to spinel reflections and the rhombuses to hematite. (For interpretation of the references to colour in this figure legend, the reader is referred to the web version of this article).

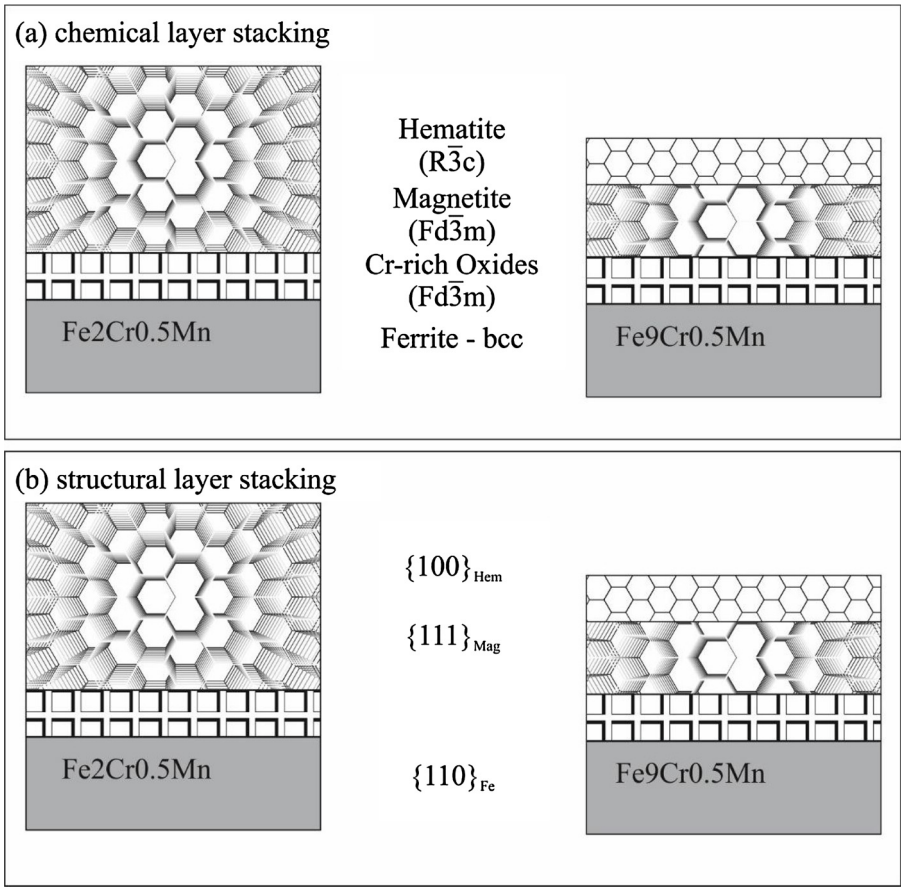

Fig. 8. Layer stacking of oxide corrosion products as observed by EBSD and TEM from a) a chemical perspective and b) a structural perspective.

the stable reaction product at the oxide/gas interface should be hematite [17,18,27]. This oxide was only observed on the higher alloyed material Fe9Cr0.5 Mn. The orientation relationships observed for ferrite and the iron oxides for the two different alloys were:

- Fe2Cr0.5 Mn: $\{110\}_{Fe}\|\{111\}_{Mag}$
- Fe9Cr0.5 Mn: $\{110\}_{Fe}\|\{100\}_{Hem}$

For Fe9Cr0.5 Mn it must be considered, hematite is the top layer and magnetite the layer in contact with ferrite. Magnetite acts as a structural mediator between ferrite and hematite.

In order to evaluate the structural and orientation relationships, the crystal structures of ferrite and the dominating metal oxides are revisited.

4.1. Orientation relations

The ferritic model alloys are characterized by a *bcc* lattice of iron with partially chromium occupying the *bcc* sites. Magnetite, growing on ferrite, crystallize in an inverse spinel (space group Fd-3 m) with a closed packed (*fcc*) oxygen sub-lattice. Divalent and trivalent iron are occupying the tetrahedral and octahedral voids of the cubic closed packed lattice. Fe^{2+} only occupies the tetrahedral voids and Fe^{3+} both, the tetrahedral and octahedral, voids of the oxygen *fcc* lattice. The cubic space group Fd-3 m of magnetite can be arranged in a trigonal description to R-3 m.

Hematite, growing on top of magnetite on Fe9Cr0.5 Mn, forms a hexagonal unit cell, consisting of a hexagonal closed packed (*hcp*) oxygen sub-lattice along the [001] direction. Fe^{3+} ions fill 2/3 of the octahedral interstices within the *hcp* sub-lattice [28,29]. Fig. 9 shows the oxygen sub-lattices for magnetite along the [111] and for hematite along the [001] directions. Oxygen forms in both structures closed packed arrangements. From this it follows, that the structural transition from magnetite to hematite makes use of iron diffusion only, via the octahedral and tetrahedral voids within the closed packed oxygen lattices. The representation of the trigonal cell within the magnetite structure along the [111] direction and the [001] projection of hematite illustrates the structural similarities between both iron oxides. A small lattice mismatch for this orientation relation is expected.

4.2. Fe2Cr0.5 Mn

The EBSD analysis before and after oxidation indicates an epitaxial relation between the base alloy (Fe2Cr0.5 Mn) and the oxide (magnetite) formed on the surface. The TEM cross sectional analysis demonstrated a Cr-rich layer at the alloy/oxide interface. The existence of a magnetite layer with chromium dissolved in the magnetite structure is likely to be observed for low alloyed Fe-Cr alloys. Previous investigations showed, this layer is not a pure chromite ($FeCr_2O_4$) layer and corresponds to a $(Fe,Cr)_3O_4$ layer [30]. To evaluate the observations by EBSD, the lattice mismatch was calculated with the lattice constants of ferrite (a_F = 2.867 Å) and magnetite (a_M = 8.405 Å; according to International Crystal Structure Database (ICSD) entry #165105) for three different orientation relations. The lattice arrangement is displayed for the three different cases A: $< 100 >_{Fe}\| < 100 >_{M}$; B: $< 111 >_{Fe}\| < 110 >_{M}$ and C: $< 110 >_{Fe}\| < 111 >_{M}$ in Fig. 10. Using the plane diagonal of the *bcc* lattice of ferrite (**c**) and of the *fcc* sub-lattice of oxygen (**d**) from magnetite, the lattice distances imaged in Fig. 10 can be calculated by

$$c, d1 = a_{F,M} \quad (1)$$

$$c, d2 = \sqrt{2}\, a_{F,M} \quad (2)$$

$$c, d3 = \sqrt{(\sqrt{2}\, a_{F,M})^2 - (\frac{\sqrt{2}\, a_{F,M}}{2})^2} \quad (3)$$

The strain in % is then defined by:

$$strain\ in\ \% = \frac{100 \bullet (d - c)}{c} \quad (4)$$

As observed in Fig. 10 it is convenient to evaluate the distance relations taking the ferrite lattice distances times three, compared to magnetite. Table 2 summarizes the observed orientation relationships and their mismatch for the epitaxial growth of magnetite on ferrite. The figure displays the view along the z-direction.

For case (A), ferrite grains with originally [100] orientation would develop magnetite with [100] orientation in z-direction. The lattice mismatch for this relation is only 0.98, resulting in a strain of 2.27 %. (see Fig. 10 (A)). The orientation relations for the cases (B) and (C) result in the same values. The lattice mismatch and strain are equal for all cases. Therefore, the relations observed by EBSD $< 110 >_{Fe}\| < 111 >_{M}$ demonstrate the observed situation characterized by following the closed packed arrangements to minimize the interfacial

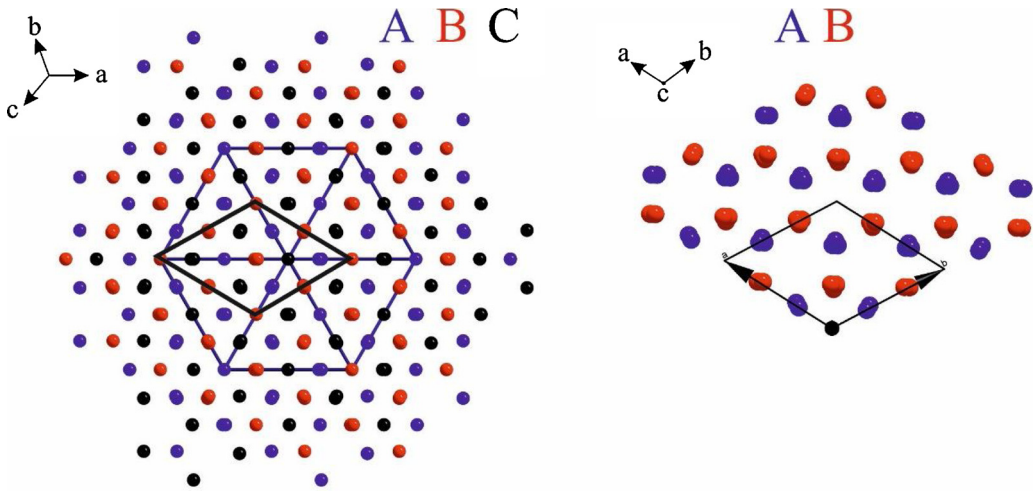

Fig. 9. Closed packed oxygen sub-lattices of magnetite and hematite. For magnetite, the cubic (blue) and the trigonal (black) unit cells are shown. (For interpretation of the references to colour in this figure legend, the reader is referred to the web version of this article).

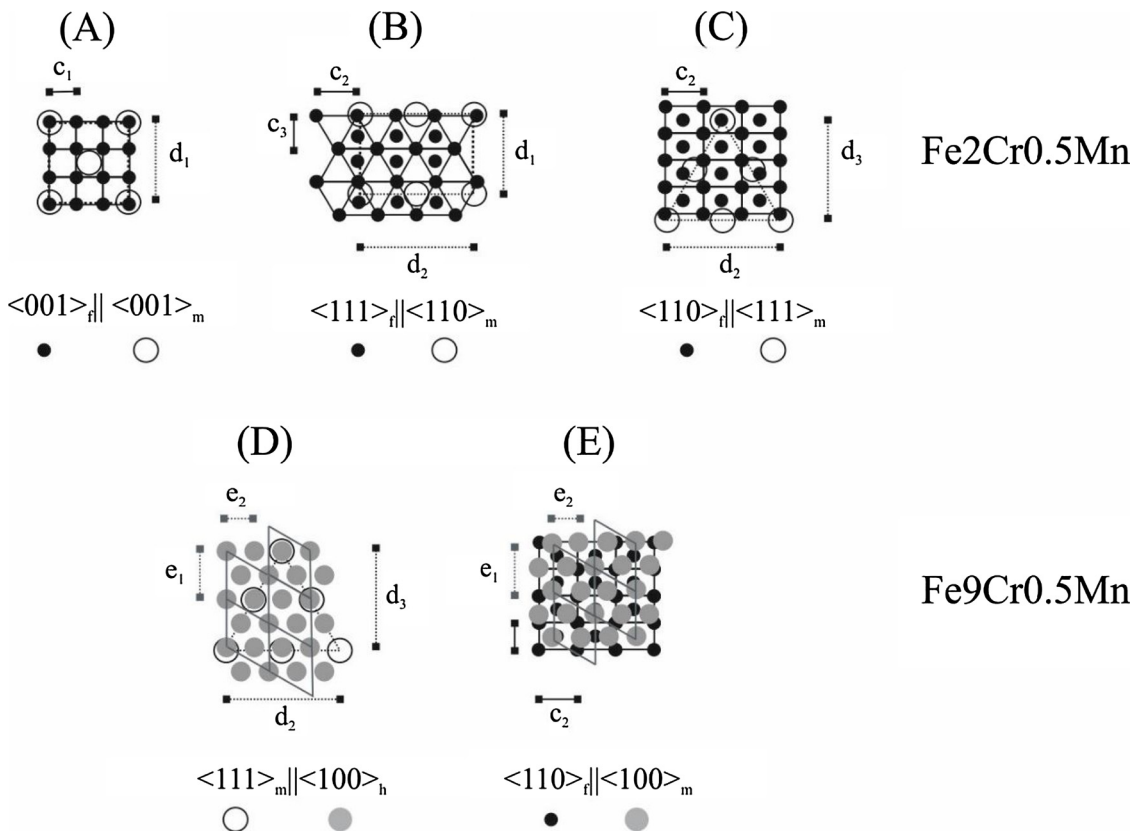

Fig. 10. Illustration of lattice mismatch: In cases (A) to (C) open circles correspond to *fcc* oxygen sub lattice of magnetite, full circles belong to *bcc* lattice of iron in ferrite. For the cases (D) and (E) grey filled circles correspond to oxygen sub-lattice of hematite. Lattice distances marked as **c** correspond to ferrite, **d** to magnetite and **e** to hematite.

Table 2
Calculated lattice misfit for the different orientation relations as observed for Fe2Cr0.5 Mn and Fe9Cr0.5 Mn.

Case	orientation relation	lattice plane distance relation	Strain in %
(A)	$< 100 >_f \,\|\|\, < 100 >_m$	$\frac{d_1}{3 \cdot dc_1} \approx 0.98$	2.27
(B)	$< 111 >_f \,\|\|\, < 110 >_m$	$\frac{d_2}{3 \cdot c_2} \approx 0.98$	2.27
(C)	$< 110 >_f \,\|\|\, < 111 >_m$	$\frac{d_2}{3 \cdot c_2} \approx 0.98$	2.27
(D)	$< 111 >_m \,\|\|\, < 001 >_h$	$\frac{4 \cdot e_2}{d_2} \approx 0.98$	2.35
		$\frac{5 \cdot e_1}{d_3} \approx 0.98$	2.23
(E)	$< 110 >_f \,\|\|\, < 100 >_h$	$\frac{4 \cdot e_2}{3 \cdot c_2} \approx 0.96$	4.29
		$\frac{e_1}{2 \cdot c_1} \approx 0.88$	12.06

energies between the base alloy and reaction products for nucleation and growth.

On Fe2Cr0.5 Mn only magnetite was observed after 2 min of exposure and no hematite on top of the magnetite layer. As observed by the inspection of the structural relations, iron outward diffusion is the key part for the transformation from magnetite to hematite. As observed by in-situ experiments previously [15,27], the growth of hematite is delayed compared to magnetite formation. The specimen of this study was only exposed for 2 min and it is expected, that the time for outward diffusion of iron towards the gas interface was too short to form hematite.

4.3. Fe9Cr0.5 Mn

The EBSD surface analysis of Fe9Cr0.5 Mn exposed to SO_2 at 650 °C for 5 min demonstrated a mixed external oxide layer with magnetite on ferrite and hematite at the gas/oxide interface. In Fig. 9 (a) and (b) the structural relations for the layer stacking of oxygen sub-lattices of magnetite and hematite is demonstrated.

Using the lattice distances (**e**) of the *hcp* sub-lattice of hematite imaged in Fig. 10, the different values can be calculated by:

$$e1 = a_H = 5.036\text{Å} \tag{5}$$

$$e2 = \frac{\sqrt{3a_H^2}}{3} = 2.907\text{Å} \tag{6}$$

with $\boldsymbol{a_H}$ being the lattice parameter of hematite (according to *International Crystal Structure Database* – ICSD entry #161290).

The growth of hematite directly on ferrite would lead to a strain of 4–12 %. This high strain makes it unlikely to form a trigonal oxide structure such as hematite or chromia directly on ferrite, due to structural reasons. The critical aspect for chromia formation in an alloy with only 9 percent by weight chromium is thus mainly the chemical potential of chromium at the interface between gas and alloy. Below the hematite layer magnetite was observed by TEM cross-sectional analysis. Magnetite acts as a structural mediator between ferrite and hematite. The inner oxidation zone shows a high degree of porosity and a mixed Fe-Cr-oxide layer. Hematite with [001] orientation grew on ferrite grains with [101]-orientation. The strain for the direct epitaxial growth of hematite on ferrite would be 4 %. Ferrite grains of the Fe9Cr0.5 Mn sample with [101]-orientation show magnetite grains with [111]-orientation in z-direction. This leads to the assumption of an orientation relation of hematite [001] and magnetite [111], which is supported by the structural relations as discussed previously. The fitting of the lattice planes for this case (D) is demonstrated in Fig. 10. The calculated misfit of this setting is about 2 %. Since a direct growth of hematite on top of ferrite cannot be excluded, a theoretical crystal plane fitting is shown in case (E). The misfit with 4 % to 12 % for this fitting is larger compared

Table 3
Atomic density of basic planes of the cubic bcc lattice.

Basic plane	No. of atoms N	Area in a^2	Atomic Density N^{*a-2}
{100}	1	1	1
{110}	2	1.41	1.41
{111}	0.5	1.73	0.29

[a] Lattice parameter.

to the ferrite-magnetite-hematite fitting and is despite thermodynamic reasons unlikely to be observed due to structural reasons.

4.4. General remarks

This comprehensive analysis of orientation relations for corrosion products on ferritic alloys suggests the following consecutive stacking:

On ferrite $< 110 >$ magnetite forms with $< 111 >$ orientation. With higher Cr-content in the alloy hematite is observed at the oxide/gas interface. This hematite layer grows preferentially with [001] orientation on magnetite with [111] orientation. This observation is supported by the structural similarities between magnetite and hematite, when using the trigonal notation of magnetite. Ferrite grains with [101] orientations are favoured for magnetite growth, due to the atomic density of the lattice planes. Table 3 shows the atomic density of the three basic planes in the *bcc* lattice of ferrite. The highest atomic density is found in the (110) lattice plane. Atoms on the surface of a crystal naturally have less neighbors than the atoms inside the crystal. Due to their effort to replace these missing bonds, they have a high reactivity. As a result, orientations of the ferrite grains with a higher atomic density tend to form more bonds to the reactive gas and thus being the preferred nucleation site of the corrosion products.

Since the present study only considers the first minutes of the reaction of Fe-Cr alloys in hot SO_2-containing atmosphere, it seems difficult from the authors point of view to estimate to what extent the epitaxial growth will develop over a longer period of time. It can be state that a spinel-like phase of the type $(Fe,Cr)_3O_4$ is formed on Fe2Cr0.5 Mn, which follows over-proportionally the growth law $\{110\}_f \,||\{111\}_m$ and $< 111 >_f \,|| < 110 >_m$. With Fe9Cr0.5 Mn on the other hand, a [001]-oriented hematite is observed by EBSD after this time. According to TEM cross sectional analysis (see Fig. 7) directly at the interface, a spinel-like phase also forms as an intermediate stage in the case of Fe9Cr0.5 Mn, and that the hematite is only formed as the cation concentration decreases. Between the spinel and the magnetite, the dense oxygen packing only must change from *fcc* to *hcp*, respectively, which incidentally is associated with a slight reduction in volume. This conversion is pre-interpreted as the result of cation diffusion, which should be associated with an inhomogeneous and disordered cation distribution from the non-equilibrium process. Furthermore, the space change processes necessary in phase transformation as well as the speed of growth suggest that a sufficient amount of lattice defects will be incorporated, which may lead to further weakening of the texture, supported by nucleation and growth of new oxide grains. Thus, the epitaxial growth via the texture in the alloy, but also the defect structure in the cation sub-lattice can influence the global texture. Which effect dominates where over longer exposure time can only be proven by further studies.

The strain relations should be considered for the desired growth of a chromia layer on ferritic high temperature alloys. Chromia growth is mainly affected by the critical chromium content at the alloy/gas interface. Additionally, chromia is structurally very similar to hematite. Hematite and chromia both crystallize in space group R-3c and the oxygen sublattice follows a hexagonal closed packing (*hcp*). The lattice parameters *a* and *c* of chromia are only slightly smaller compared to hematite ($a_H = 5.036$ Å and $c_H = 13.781$ Å; $a_{Chr} = 4.957$ Å and $c_{Chr} = 13.592$ Å) according to *International Crystal Structure Database* (ICSD) entry #75577 for Cr_2O_3 and #161290 for Fe_2O_3. The structural similarities between oxide crystal phases is described in more detail by Nolze et al. [29]. The strain relations between chromia and ferrite can be considered in approximation to the relations between ferrite and hematite. A reduction of strain between the two species (alloy and chromia) may be another factor to tune, in order to force an alloy containing only 9 percent by weight in chromium to form a dense and protective chromia layer.

The EBSD analysis only recorded signals from the oxides as reaction products after the short time SO_2 exposure. The subsequent TEM cross-sectional analysis demonstrated sulphur accumulation in the external corrosion zone on Fe2Cr0.5 Mn. The time of exposure was not sufficient to generate crystalline sulphides in the corrosion zones of Fe9Cr0.5 Mn. Studies that have analyzed sulphidation over a longer period of time indicate that the sulphides primarily crystallize separately, next to the oxides, or at the grain boundaries of the base material [12,18,27]. In the case of the generation of oxygen vacancies in the oxide with a longer exposure time at the metal/oxide interface, sulphur can take up space on the oxygen vacancies. No evidence for this could be found in this study. After the analysis of the orientation relations between oxides and the underlying base alloy, sulphur is not expected to play a role for the development of the epitaxial relations described here.

5. Conclusions

The present work demonstrates epitaxial relations between metallic alloys and the resulting oxide reaction products for the case of hot corrosion of Fe-Cr alloys in SO_2 containing atmosphere. Vickers' indentation was used to mark the alloy prior to the exposure experiments to study equivalent areas before and after corrosion by EBSD. This study demonstrates the initial stages of corrosion, and the growth process, which is dominated by structural relations between the closed packed lattices. The main findings can be summarized as follows:

- For Fe2Cr0.5 Mn a clear epitaxial relationship of magnetite and ferrite with $< 110 >_f \,|| < 111 >_m$ was observed.
- For Fe9Cr0.5 Mn, a mixed hematite-magnetite layer with hematite at the gas/oxide interface was observed and magnetite with cubic spinel type crystal structure acts as a structural mediator.
- On Fe9Cr0.5 Mn hematite above [101]-ferrite has a clear [001]-orientation in z-direction and the layer growth mainly proceeds by outward cation diffusion through the closed packed oxygen sublattices of magnetite and hematite.

However, for the oxide layer growth on Fe9Cr0.5 Mn it is demonstrated that the most hematite crystals grow with [001]-orientation in z-direction with low deviations. Looking at the strain between the lattice planes and the preferred crystal plane fittings illustrates that having an atomic bonding partner from the new phase is more important than a low misfit of lattice spacing's. Regarding the field of SO_2 corrosion the study demonstrates clearly, that the reaction products follow the rule of closed packed lattice planes for layer growth. The approach of studying structural characteristics of oxide layers after corrosion by surface EBSD analysis may give valuable insights into other scientific areas such as aqueous corrosion.

Data availability

The raw/processed data required to reproduce these findings cannot be shared at this time as the data also forms part of an ongoing study.

CRediT authorship contribution statement

Christiane Stephan-Scherb: Conceptualization, Methodology, Writing - review & editing, Visualization, Supervision, Data curation. **Martina Menneken:** Methodology, Investigation, Writing - review & editing. **Kathrin Weber:** Methodology, Investigation, Writing - original

draft. **Leonardo Agudo Jácome:** Investigation, Writing - review & editing. **Gert Nolze:** Investigation, Validation, Writing - review & editing.

Declaration of Competing Interest

The authors declare that they have no known competing financial interests or personal relationships that could have appeared to influence the work reported in this paper.

Acknowledgement

The authors gratefully acknowledge Romeo Saliwan-Neumann for the extensive EBSD analysis, as well as Anna Manzoni and Wencke Schulz for consequent proof-reading and valuable discussions.

Appendix A. Supplementary data

Supplementary material related to this article can be found, in the online version, at doi:https://doi.org/10.1016/j.corsci.2020.108809.

References

[1] D. Young, High Temperature Oxidation and Corrosion of Metals, Elsevier, 2016.
[2] K. Chandra, A. Kranzmann, R.S. Neumann, G. Oder, F. Rizzo, High temperature oxidation behavior of 9-12 % Cr ferritic/martensitic steels in a simulated dry oxyfuel environment, Oxid. Met. 83 (2015) 291–316.
[3] J.P. Abellan, T. Olszewski, H.J. Penkalla, G.H. Meier, L. Singheiser, W.J. Quadakkers, Scale formation mechanisms of martensitic steels in high CO2/H2O-containing gases simulating oxyfuel environments, Mater. High Temp. 26 (2009) 63–72.
[4] F. Gesmundo, C.D. Asmundis, S. Merlo, C. Bottino, Corrosion of Iron in pure So2 under different pressures at 700-Degrees-C, Werkst. Korros. 30 (1979) 179–185.
[5] N. Birks, G.H. Meier, F.S. Pettit, Introduction to the High-Temperature Oxidation of Metals, 2nd edition, Introduction to the High-Temperature Oxidation of Metals, 2006, pp. 1–338.
[6] J.-H. Kim, B.K. Kim, D.-I. Kim, P.-P. Choi, D. Raabe, K.-W. Yi, The role of grain boundaries in the initial oxidation behavior of austenitic stainless steel containing alloyed Cu at 700°C for advanced thermal power plant applications, Corros. Sci. 96 (2015) 52–66.
[7] N. Cabrera, N.F. Mott, Theory of the oxidation of metals, Rep. Prog. Phys. 12 (1949) 163–184.
[8] C. Wagner, Equations for transport in solid oxides and sulfides of transition metals, Prog. Solid State Chem. 10 (1975) 3–16.
[9] L.L. Luo, L.F. Zou, D.K. Schreiber, D.R. Baer, S.M. Bruemmer, G.W. Zhou, C.M. Wang, In-situ transmission electron microscopy study of surface oxidation for Ni-10Cr and Ni-20Cr alloys, Scripta Mater. 114 (2016) 129–132.
[10] W.H. Blades, P. Reinke, From alloy to oxide: capturing the early stages of oxidation on Ni-Cr(100) alloys, Acs Appl. Mater. Interface 10 (2018) 43219–43229.
[11] T.D. Reynolds, D.M. Collins, N.K. Soor, S.R. Street, N. Warnken, P.M. Mignanelli, M.C. Hardy, H.E. Evans, M.P. Taylor, Identifying heating rate dependent oxidation reactions on a nickel-based superalloy using synchrotron diffraction, Acta Mater. 181 (2019) 570–583.
[12] C. Stephan-Scherb, K. Nutzmann, A. Kranzmann, M. Klaus, C. Genzel, Real time observation of high temperature oxidation and sulfidation of Fe-Cr model alloys, Mater. Corros. 69 (2018) 678–689.
[13] L. Latu-Romain, Y. Parsa, S. Mathieu, M. Vilasi, Y. Wouters, Chromia scale thermally grown on pure chromium under controlled p(O-2) atmosphere: I. Spallation investigation using photoelectrochemical techniques at a mesoscale, Oxid. Met. 90 (2018) 255–266.
[14] L. Latu-Romain, Y. Parsa, S. Mathieu, M. Vilasi, Y. Wouters, Chromia scale thermally grown on pure chromium under controlled p(O-2) atmosphere: II spallation investigation using photoelectrochemical techniques at a microscale, Oxid. Met. 90 (2018) 267–277.
[15] Y. Parsa, L. Latu-Romain, Y. Wouters, S. Mathieu, T. Perez, M. Vilasi, Effect of oxygen partial pressure on the semiconducting properties of thermally grown chromia on pure chromium, Corros. Sci. 141 (2018) 46–52.
[16] P. Huczkowski, T. Olszewski, M. Schiek, B. Lutz, G.R. Holcomb, V. Shemet, W. Nowak, G.H. Meier, L. Singheiser, W.J. Quadakkers, Effect of SO2 on oxidation of metallic materials in CO2/H2O-rich gases relevant to oxyfuel environments, Mater. Corros. 65 (2014) 121–131.
[17] P. Huczkowski, D.J. Young, T. Olszewski, A. Chyrkin, W.J. Quadakkers, Effect of sulphur on the oxidation behaviour of possible construction materials for heat exchangers in oxyfuel plants in the temperature range 550-700 degrees C, Oxid. Met. 89 (2018) 651–681.
[18] K. Nützmann, A. Kranzmann, C. Stephan-Scherb, The influence of chromium on early high temperature corrosion of ferritic alloys under SO2 atmosphere, Mater. High Temp. 35 (2018) 558–568.
[19] Z. Zurek, J. Gilewicz-Wolter, M. Hetmanczyk, J. Dudala, A. Stawiarski, High temperature corrosion of chromium-manganese steels in sulfur dioxide, Oxid. Met. 64 (2005) 379–395.
[20] H. Kirsch, Zur Kristallchemie der Magnetitschutzschichten in den Stahlrohren von Hochdruckdampf-Kraftwerken, Archiv für das Eisenhüttenwesen 36 (1965) 603–608.
[21] W.E. Boggs, R.H. Kachik, Pellissi Ge, Effect of oxygen pressure on oxidation of zone-refined Iron, J. Electrochem. Soc. 112 (1965) 539-&..
[22] P.B. Sewell, M. Cohen, The oxidation of Iron Single crystals around 200-degrees-C, J. Electrochem. Soc. 111 (1964) 501–508.
[23] C. Leygraf, G. Hultquist, Initial oxidation stages on Fe-Cr(100) and Fe-Cr(110) surfaces, Surf. Sci. 61 (1976) 69–84.
[24] R.P. Oleksak, J.P. Baltrus, J. Nakano, A. Nakano, G.R. Holcomb, O.N. Dogan, Mechanistic insights into the oxidation behavior of Ni alloys in high-temperature CO2, Corros. Sci. 125 (2017) 77–86.
[25] R.P. Oleksak, M. Kapoor, D.E. Perea, G.R. Holcomb, Ö.N. Doğan, The role of metal vacancies during high-temperature oxidation of alloys, Npj Mater. Degrad. 2 (2018) 25.
[26] C. Juricic, H. Pinto, D. Cardinali, M. Klaus, C. Genzel, A.R. Pyzalla, Evolution of microstructure and internal stresses in multi-phase oxide scales grown on (110) surfaces of Iron Single crystals at 650 °C, Oxid. Met. 73 (2010) 115–138.
[27] F. Falk, M. Menneken, C. Stephan-Scherb, Real-time observation of high-temperature gas corrosion in dry and wet SO2-Containing atmosphere, Jom-Us 71 (2019) 1560–1565.
[28] R.M. Cornell, U. Schwertmann, The Iron Oxides, Wiley-VCH Verlag GmbH & Co.KGaA, Weinheim, 2003.
[29] G. Nolze, A. Winkelmann, Exploring structural similarities between crystal phases using EBSD pattern comparison, Cryst. Res. Technol. 49 (2014) 490–501.
[30] K. Weber, A.G. Buzanich, M. Radtke, U. Reinholz, C. Stephan-Scherb, A mu-XANES study of the combined oxidation/sulfidation of Fe-Cr model alloys, Mater. Corros. 70 (2019) 1360–1370.